Boundary Layer Instabilities Over a Cone-Cylinder-Flare Model at Mach 6

P. Paredes,[1] A. Scholten,[2] M. Choudhari,[3] F. Li,[3]
E. Benitez,[4] J. Jewell[5]

[1]National Institute of Aerospace

[2]North Carolina State University

[3]Computational AeroSciences Branch, NASA Langley Research Center

[4]U.S. Air Force Research Laboratory, WPAFB

[5]Purdue University

AIAA Scitech 2022, Jan 3-7, 2022, San Diego, CA

Outline

Outline

Cone-cylinder-flare experiments[1,2]

- Boeing/AFOSR Mach 6 Quiet Tunnel (BAM6QT) at Purdue University
- $AoA = 0^\circ$, sharp 5° half-angle cone, 10° half-angle flare

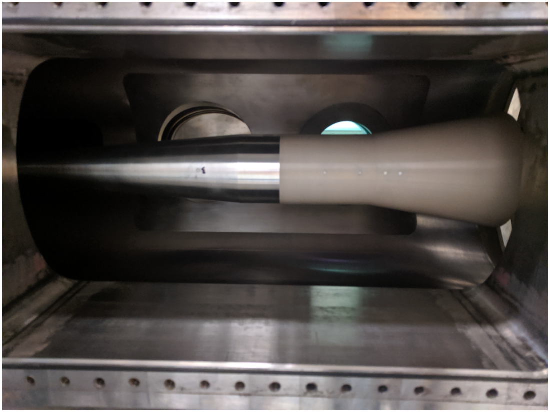

[1] E.K. Benitez et al. *Instability measurements on an axisymmetric separation bubble at Mach 6*. AIAA Paper 2020-3072. 2020.

[2] E.K. Benitez, J.S. Jewell, and S.P. Schneider. *Separation bubble variation due to small angles of attack for an axisymmetric model at Mach 6*. AIAA Paper 2021-0245. 2021.

Cone-cylinder-flare experiments[1,2]

- Boeing/AFOSR Mach 6 Quiet Tunnel (BAM6QT) at Purdue University
- $AoA = 0^\circ$, $r_n = 0.1$ mm, 5° half-angle cone, 10° half-angle flare
- $Re = 11.5 \times 10^6$ m^{-1}, $P_0 = 1.0318 \times 10^6$ Pa, $T_0 = 421.5$ K

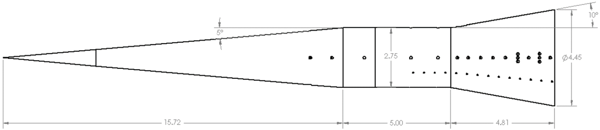

(lengths in inches)

- PCB, Kulite & FLDI

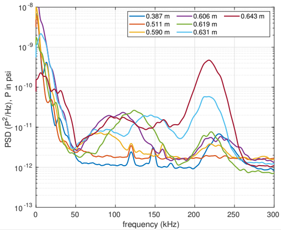

- Schlieren

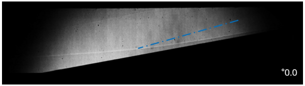

- Heat Transfer ($m = 36$)

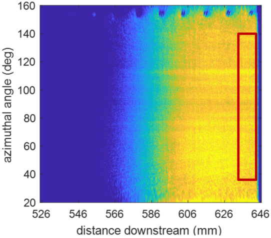

[1] E.K. Benitez et al. *Instability measurements on an axisymmetric separation bubble at Mach 6*. AIAA Paper 2020-3072. 2020.

[2] E.K. Benitez, J.S. Jewell, and S.P. Schneider. *Separation bubble variation due to small angles of attack for an axisymmetric model at Mach 6*. AIAA Paper 2021-0245. 2021.

Outline

Laminar basic state solution

- VULCAN-CFD: shock-capturing, 2^{nd}-order finite-volume NS solver
- $Re = 11.5 \times 10^6$ m^{-1}, $P_0 = 1.0318 \times 10^6$ Pa, $T_0 = 421.5$ K, $T_w = 300$ K
- $r_n =$ **0.1**, 1.0, 5.0 mm; 8°, **10°**, 12° half-angle flare
- Shock-adapted grid with 3601 × 1201 grid points
- Comparison of heat transfer for selected wall temperatures

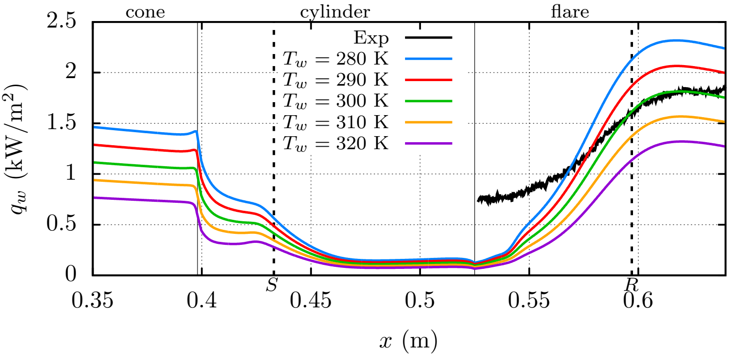

Laminar basic state solution

- VULCAN-CFD: shock-capturing, 2^{nd}-order finite-volume NS solver
- $Re = 11.5 \times 10^6$ m^{-1}, $P_0 = 1.0318 \times 10^6$ Pa, $T_0 = 421.5$ K, $T_w = 300$ K
- $r_n = \mathbf{0.1}$, 1.0, 5.0 mm; 8°, **10**°, 12° half-angle flare
- Shock-adapted grid with 3601×1201 grid points
- Mach number contours

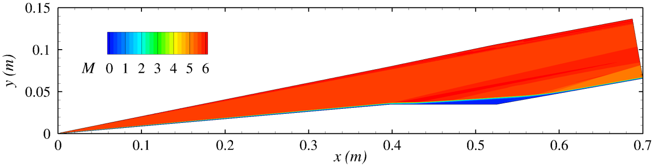

Laminar basic state solution

- VULCAN-CFD: shock-capturing, 2^{nd}-order finite-volume NS solver
- $Re = 11.5 \times 10^6$ m^{-1}, $P_0 = 1.0318 \times 10^6$ Pa, $T_0 = 421.5$ K, $T_w = 300$ K
- $r_n = \mathbf{0.1}$, 1.0, 5.0 mm; 8°, **10**°, 12° half-angle flare
- Shock-adapted grid with 3601 × 1201 grid points

- Comparison of schlieren images with density isolines

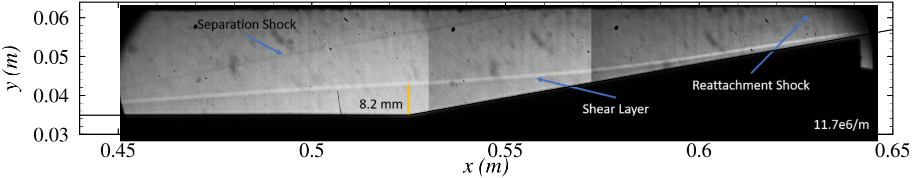

Laminar basic state solution

- VULCAN-CFD: shock-capturing, 2^{nd}-order finite-volume NS solver
- $Re = 11.5 \times 10^6$ m^{-1}, $P_0 = 1.0318 \times 10^6$ Pa, $T_0 = 421.5$ K, $T_w = 300$ K
- $r_n = \mathbf{0.1}$, 1.0, 5.0 mm; 8°, **10**°, 12° half-angle flare
- Shock-adapted grid with 3601 × 1201 grid points

- Comparison of schlieren images with density isolines

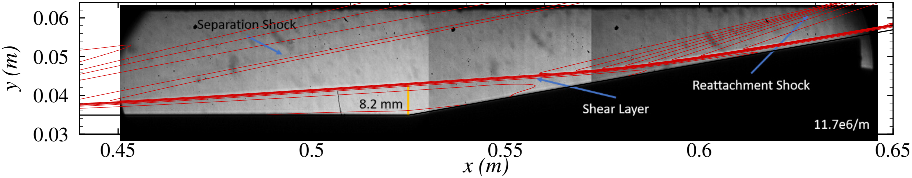

Evolution of boundary-layer convective instabilities

- PSE: boundary-layer instabilities over cone ($x \in (0, 0.39)$ m)
- HLNSE: evolution of instabilities over cylinder and flare ($x \in [0.35, 0.69]$ m)
  - inflow from PSE at $x = 0.35$ m

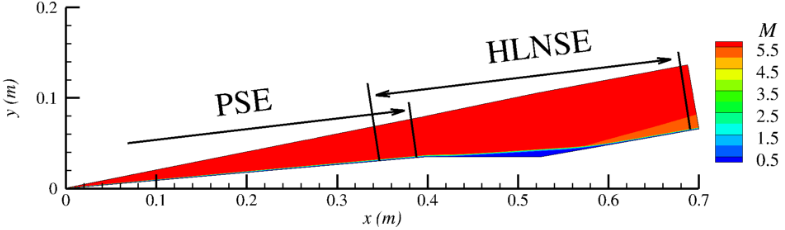

Evolution of boundary-layer convective instabilities

- $A_{p_w} = A_I \exp(N_{p_w})$, $A_I = 7.4 \times 10^{-11}$ to match measurements at $x = 0.387$ m
  - **PCB** sensor location

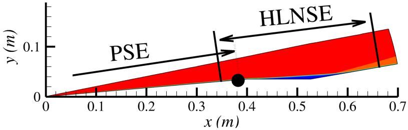

  - $\Re(\breve{u})$, $f = 60$ kHz, $m = 20$

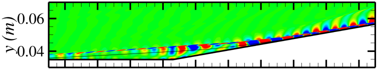

  - $\Re(\breve{u})$, $f = 210$ kHz, $m = 0$

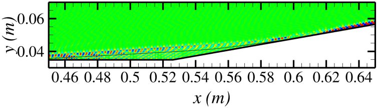

- Comparison at $x = 0.387$ m

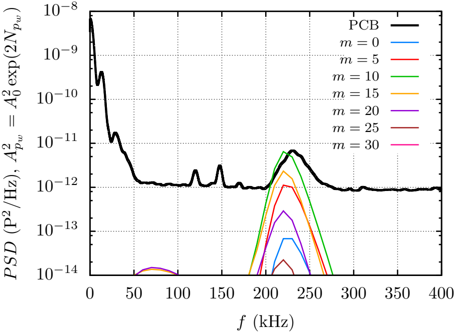

- Oblique second mode more amplified than planar due to contribution of first modes
- Oblique low frequency waves amplified along shear layer over separation

Evolution of boundary-layer convective instabilities

- $A_{p_w} = A_I \exp(N_{p_w})$, $A_I = 7.4 \times 10^{-11}$ to match measurements at $x = 0.387$ m

- **PCB** sensor location

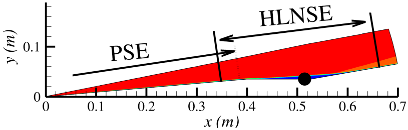

- $\Re(\breve{u})$, $f = 60$ kHz, $m = 20$

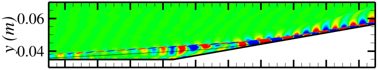

- $\Re(\breve{u})$, $f = 210$ kHz, $m = 0$

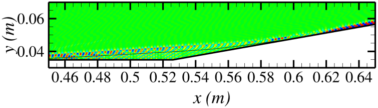

- Comparison at $x = 0.511$ m

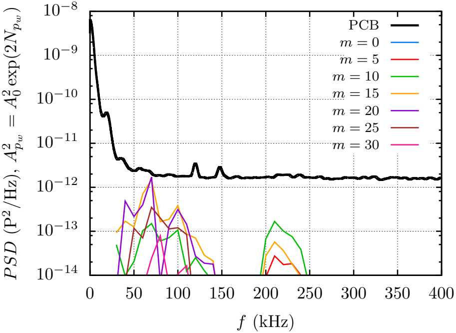

- Oblique second mode more amplified than planar due to contribution of first modes
- Oblique low frequency waves amplified along shear layer over separation

Evolution of boundary-layer convective instabilities

- $A_{p_w} = A_I \exp(N_{p_w})$, $A_I = 7.4 \times 10^{-11}$ to match measurements at $x = 0.387$ m
  - **PCB** sensor location

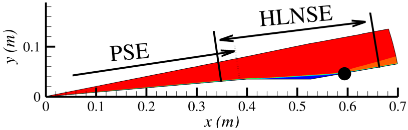

  - $\Re(\breve{u})$, $f = 60$ kHz, $m = 20$

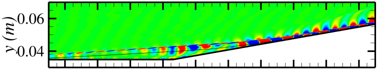

  - $\Re(\breve{u})$, $f = 210$ kHz, $m = 0$

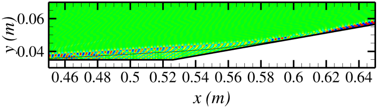

  - Comparison at $x = 0.590$ m

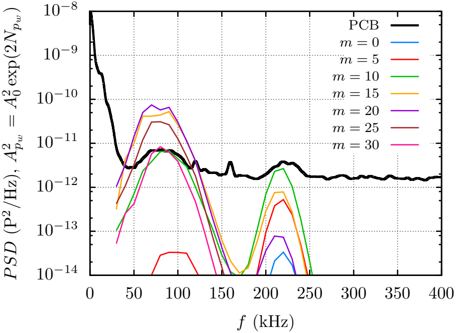

- Oblique second mode more amplified than planar due to contribution of first modes
- Oblique low frequency waves amplified along shear layer over separation

Evolution of boundary-layer convective instabilities

- $A_{p_w} = A_I \exp(N_{p_w})$, $A_I = 7.4 \times 10^{-11}$ to match measurements at $x = 0.387$ m
  - **PCB** sensor location

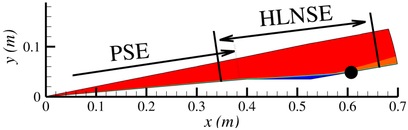

  - $\Re(\breve{u})$, $f = 60$ kHz, $m = 20$

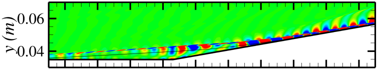

  - $\Re(\breve{u})$, $f = 210$ kHz, $m = 0$

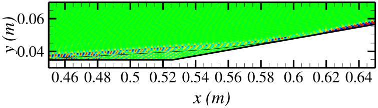

  - Comparison at $x = 0.606$ m

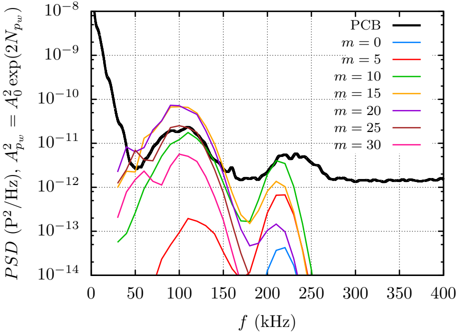

- Oblique second mode more amplified than planar due to contribution of first modes
- Oblique low frequency waves amplified along shear layer over separation

Evolution of boundary-layer convective instabilities

- $A_{p_w} = A_I \exp(N_{p_w})$, $A_I = 7.4 \times 10^{-11}$ to match measurements at $x = 0.387$ m

  - **PCB** sensor location

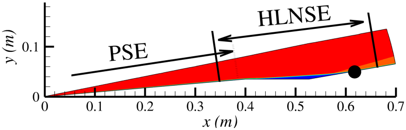

  - $\Re(\breve{u})$, $f = 60$ kHz, $m = 20$

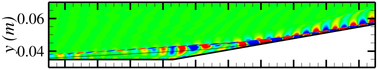

  - $\Re(\breve{u})$, $f = 210$ kHz, $m = 0$

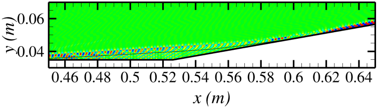

  - Comparison at $x = 0.619$ m

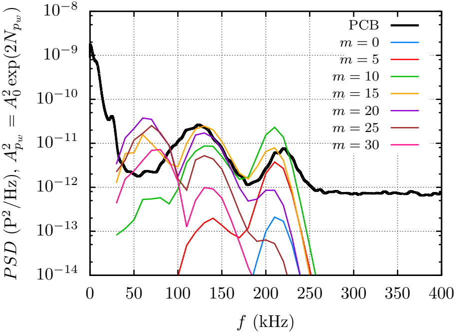

- Oblique second mode more amplified than planar due to contribution of first modes
- Oblique low frequency waves amplified along shear layer over separation

Evolution of boundary-layer convective instabilities

- $A_{p_w} = A_I \exp(N_{p_w})$, $A_I = 7.4 \times 10^{-11}$ to match measurements at $x = 0.387$ m

- **PCB** sensor location

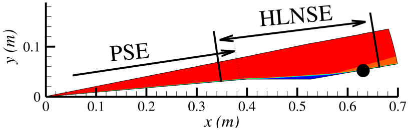

- $\Re(\breve{u})$, $f = 60$ kHz, $m = 20$

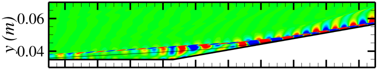

- $\Re(\breve{u})$, $f = 210$ kHz, $m = 0$

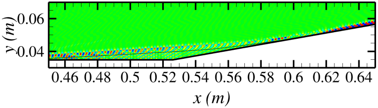

- Comparison at $x = 0.631$ m

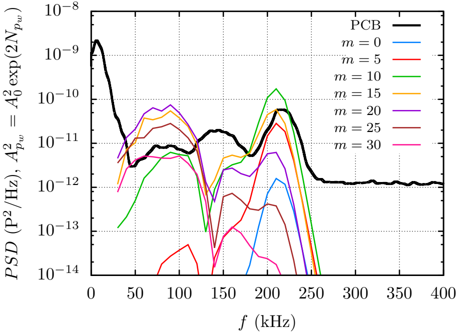

- Oblique second mode more amplified than planar due to contribution of first modes
- Oblique low frequency waves amplified along shear layer over separation

Evolution of boundary-layer convective instabilities

- $A_{p_w} = A_I \exp(N_{p_w})$, $A_I = 7.4 \times 10^{-11}$ to match measurements at $x = 0.387$ m
  - **PCB** sensor location

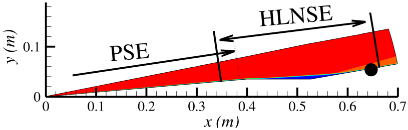

  - $\Re(\breve{u})$, $f = 60$ kHz, $m = 20$

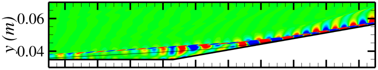

  - $\Re(\breve{u})$, $f = 210$ kHz, $m = 0$

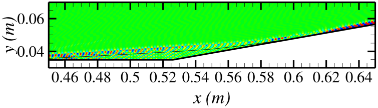

  - Comparison at $x = 0.643$ m

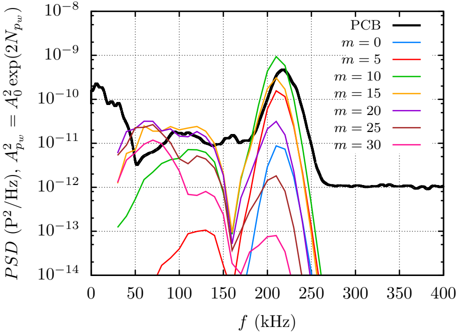

- Oblique second mode more amplified than planar due to contribution of first modes
- Oblique low frequency waves amplified along shear layer over separation

Evolution of boundary-layer convective instabilities

- $A_{p_w} = A_I \exp(N_{p_w})$, $A_I = 7.4 \times 10^{-11}$ to match measurements at $x = 0.387$ m

  - **Kulite** sensor location

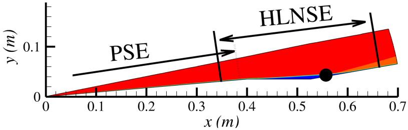

  - $\Re(\breve{u})$, $f = 60$ kHz, $m = 20$

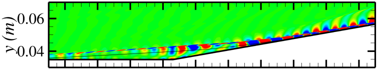

  - $\Re(\breve{u})$, $f = 210$ kHz, $m = 0$

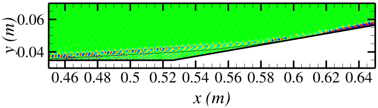

- Comparison at $x = 0.570$ m

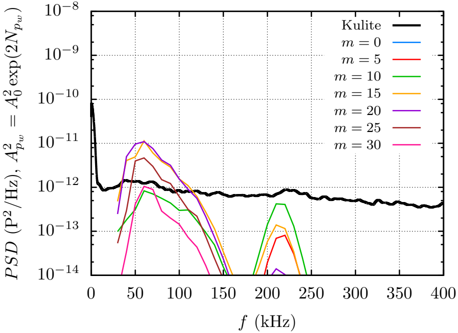

- Oblique second mode more amplified than planar due to contribution of first modes
- Oblique low frequency waves amplified along shear layer over separation

Evolution of boundary-layer convective instabilities

- $A_{p_w} = A_I \exp(N_{p_w})$, $A_I = 7.4 \times 10^{-11}$ to match measurements at $x = 0.387$ m
  - **Kulite** sensor location

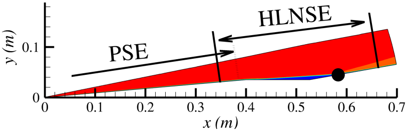

  - $\Re(\breve{u})$, $f = 60$ kHz, $m = 20$

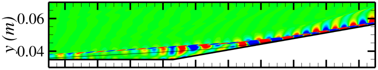

  - $\Re(\breve{u})$, $f = 210$ kHz, $m = 0$

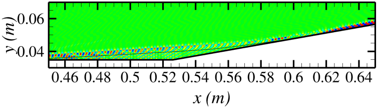

  - Comparison at $x = 0.583$ m

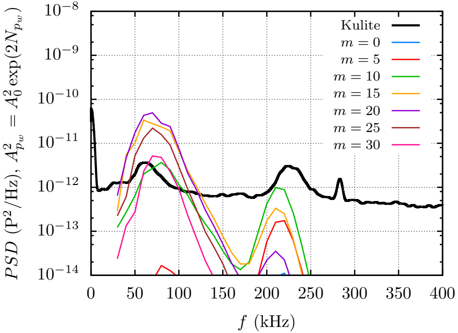

- Oblique second mode more amplified than planar due to contribution of first modes
- Oblique low frequency waves amplified along shear layer over separation

Evolution of boundary-layer convective instabilities

- $A_{p_w} = A_I \exp(N_{p_w})$, $A_I = 7.4 \times 10^{-11}$ to match measurements at $x = 0.387$ m
  - **Kulite** sensor location

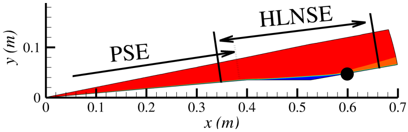

  - $\Re(\breve{u})$, $f = 60$ kHz, $m = 20$

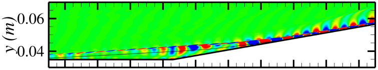

  - $\Re(\breve{u})$, $f = 210$ kHz, $m = 0$

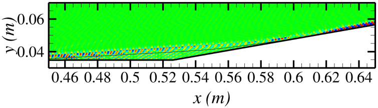

  - Comparison at $x = 0.595$ m

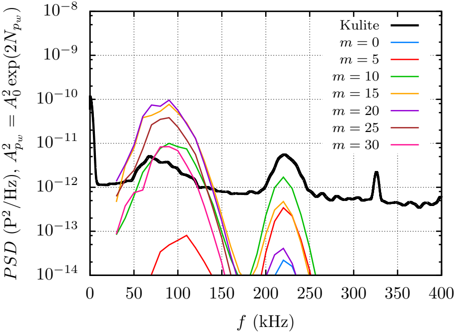

- Oblique second mode more amplified than planar due to contribution of first modes
- Oblique low frequency waves amplified along shear layer over separation

Evolution of boundary-layer convective instabilities

- $A_{p_w} = A_I \exp(N_{p_w})$, $A_I = 7.4 \times 10^{-11}$ to match measurements at $x = 0.387$ m

- **Kulite** sensor location

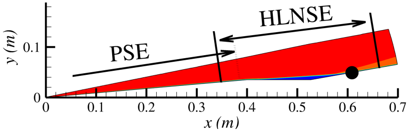

- $\Re(\breve{u})$, $f = 60$ kHz, $m = 20$

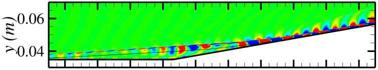

- $\Re(\breve{u})$, $f = 210$ kHz, $m = 0$

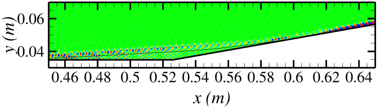

- Comparison at $x = 0.608$ m

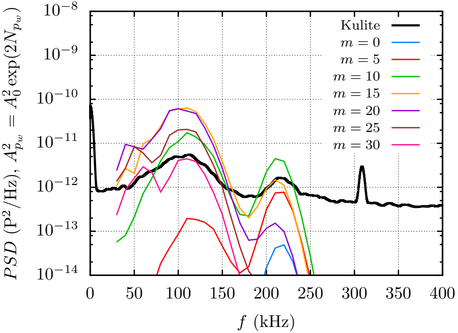

- Oblique second mode more amplified than planar due to contribution of first modes
- Oblique low frequency waves amplified along shear layer over separation

Evolution of boundary-layer convective instabilities

- $A_{p_w} = A_I \exp(N_{p_w})$, $A_I = 7.4 \times 10^{-11}$ to match measurements at $x = 0.387$ m
  - **Kulite** sensor location

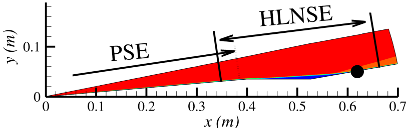

  - $\Re(\breve{u})$, $f = 60$ kHz, $m = 20$

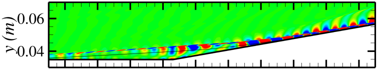

  - $\Re(\breve{u})$, $f = 210$ kHz, $m = 0$

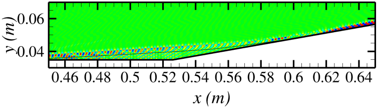

  - Comparison at $x = 0.620$ m

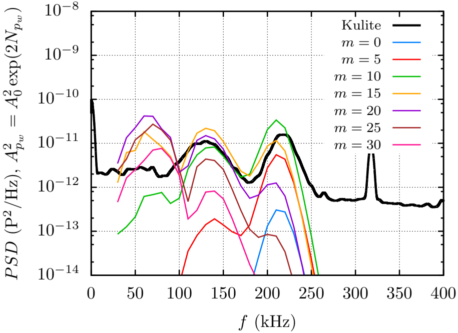

- Oblique second mode more amplified than planar due to contribution of first modes
- Oblique low frequency waves amplified along shear layer over separation

Evolution of boundary-layer convective instabilities

- $A_{p_w} = A_I \exp(N_{p_w})$, $A_I = 7.4 \times 10^{-11}$ to match measurements at $x = 0.387$ m
  - **Kulite** sensor location

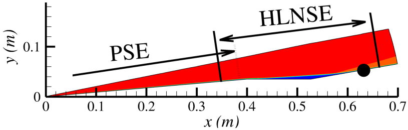

  - $\Re(\breve{u})$, $f = 60$ kHz, $m = 20$

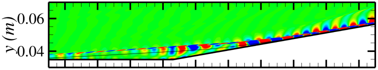

  - $\Re(\breve{u})$, $f = 210$ kHz, $m = 0$

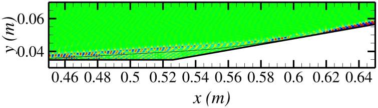

- Comparison at $x = 0.633$ m

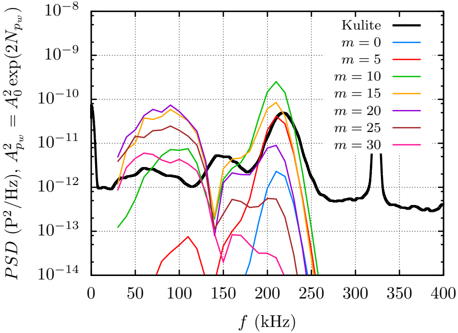

- Oblique second mode more amplified than planar due to contribution of first modes
- Oblique low frequency waves amplified along shear layer over separation

Evolution of boundary-layer convective instabilities

- $A_{p_w} = A_I \exp(N_{p_w})$, $A_I = 7.4 \times 10^{-11}$ to match measurements at $x = 0.387$ m
  - **Kulite** sensor location

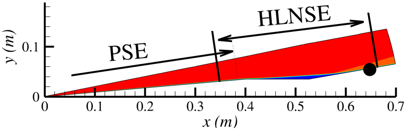

  - $\Re(\breve{u})$, $f = 60$ kHz, $m = 20$

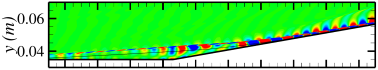

  - $\Re(\breve{u})$, $f = 210$ kHz, $m = 0$

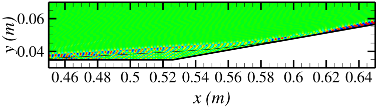

  - Comparison at $x = 0.645$ m

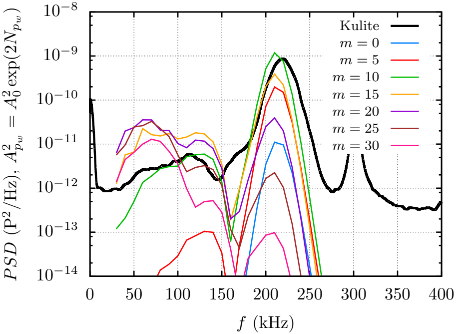

- Oblique second mode more amplified than planar due to contribution of first modes
- Oblique low frequency waves amplified along shear layer over separation

Evolution of boundary-layer convective instabilities

- Effect of nose-tip radius and flare angle on N-factor envelope
  - Planar waves ($m = 0$)
  - Oblique waves ($m = 20$)

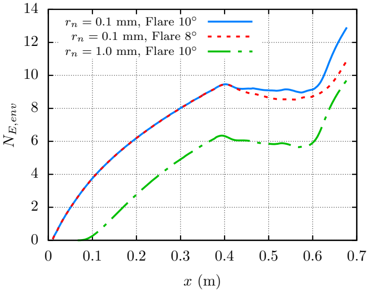

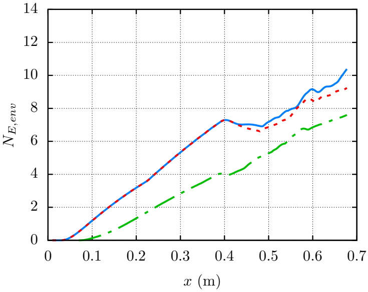

- Flare half-angle destabilizes planar and oblique waves along cylinder and flare
- Nosetip bluntness ($r_n = 1$ mm)
  - stabilizes planar and oblique waves along the cone
  - has limited effect on planar waves along cylinder-flare
  - enhances amplification of oblique waves over separated region

Evolution of boundary-layer convective instabilities

- Effect of nose-tip radius and flare angle on N-factor envelope
  - Planar waves ($m = 0$)

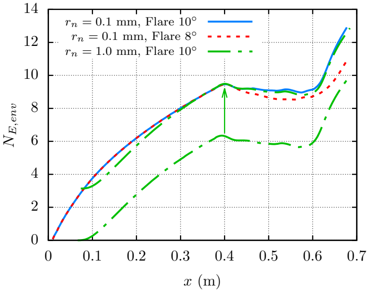

  - Oblique waves ($m = 20$)

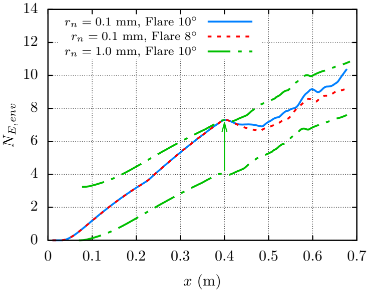

- Flare half-angle destabilizes planar and oblique waves along cylinder and flare
- Nosetip bluntness ($r_n = 1$ mm)
  - stabilizes planar and oblique waves along the cone
  - has limited effect on planar waves along cylinder-flare
  - enhances amplification of oblique waves over separated region

Self-excited global instabilities

- Global EVP: self-excited instabilities over cylinder and flare ($x \in [0.35, 0.69]$ m)

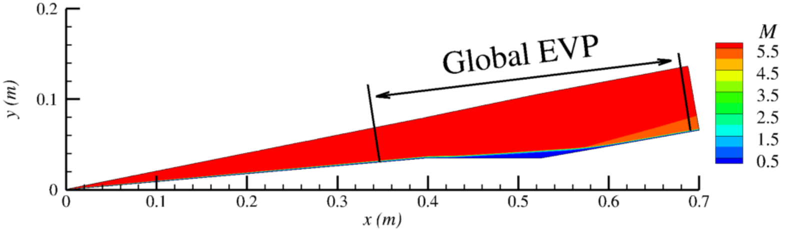

Global instabilities

- Global instability analysis performed over separation region ($x \in [0.35, 0.69]$ m)
- Effect of nose-tip radius and flare angle
  - Growth rate, $\sigma = \Im(\Omega)$

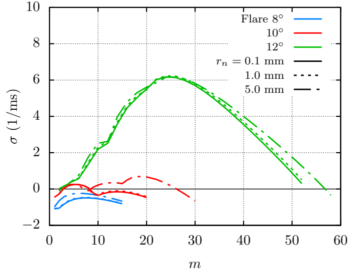

- $\Re(\hat{w})$, 10° half-angle flare ($m = 5$)

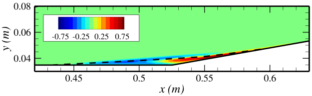

- $\Re(\hat{w})$, 12° half-angle flare ($m = 25$)

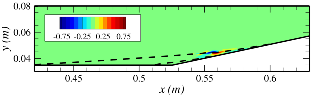

- Unstable mode for 10° flare also found in Mach 5 flow over slender double wedge[3]
  - Growth rate peak for $\lambda_z / L_{sep} \approx 0.26$ for both configurations
- Strong unstable mode for 12° half-angle flare with $\max(\sigma)$ at $m = 25$ ($\lambda = 14.4°$)
- Nosetip bluntness destabilizes separated flow (notable for 10° half-angle flare)

[3] S. GS et al. "Onset of three-dimensionality in supersonic flow over a slender double wedge". In: *Physical Review Fluids* 3.093901 (2018), pp. 1–29. DOI: 10.1103/PhysRevFluids.3.093901.

Temporal Evolution of Global Instabilities

- High-order WENO-based DNS for 10° half-angle flare with $\lambda = 60^\circ$
- Grid: $402 \times 48 \times 513$
- Simulation started with axisymmetric solution $+\ \epsilon \times$ global mode: $\bar{\mathbf{q}} + 10^{-5}\tilde{\mathbf{q}}/||\tilde{\mathbf{q}}||$
  - Simulation setup

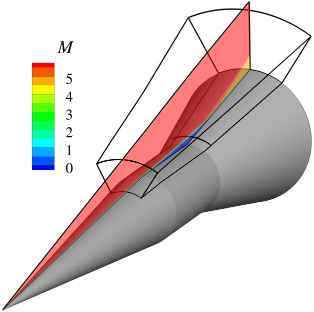

- Evolution of $\tilde{w}$ for all ζ points at $x = 0.543$ m, $\eta = 0.001$ m

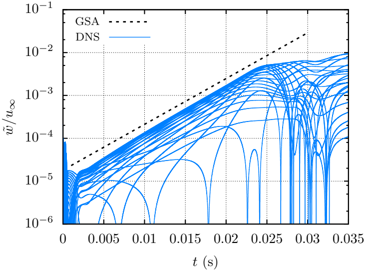

- Global mode amplifies with the predicted linear growth rate until nonlinear effects become important[4]

[4] F. Li et al. *Nonlinear evolution of instabilities in a laminar separation bubble at hypersonic Mach number*. submitted to AIAA Aviation 2022. 2022.

Outline

Concluding remarks

- Remarkable agreement with heat transfer measurements, but only downstream of reattachment
- Distinct lobes of disturbance amplification in measured p' spectra captured in computational analysis, but some differences in amplification characteristics at low frequencies
- Oblique instabilities predicted to play an important role in overall disturbance amplification
- 10° half-angle flare found to be globally unstable (3D stationary mode)
- Experimental measurements with lower & higher flare angles would be useful
  - 8° half-angle flare: subcritical to global instabilities and axisymmetric
  - 12° half-angle flare: strong global instabilities and becomes 3D and unsteady

Thank you for your attention

- Acknowledgments

  - This research was sponsored in part by the NASA Hypersonic Technology Project (HTP) under the Aeronautics Research Mission Directorate (ARMD) and by the U. S. Office of Naval Research (ONR) under award number N00014-20-1-2261 with P.O. Eric Marineau.
  - Resources supporting this work were provided by the DoD High Performance Computing Modernization Program, the NASA High-End Computing (HEC) Program through the NASA Advanced Supercomputing (NAS) Division at Ames Research Center and the NASA K-Midrange Cluster at Langley Research Center.
  - We thank Drs. Schneider, Kuehl, and Esquieu for various technical discussions related to this topic, as well as Mr. White and Dr. Baurle for their generous advice concerning the VULCAN-CFD computations.

Outline

Evolution of convective waves: PSE & HLNSE

- Decomposition of flow variables:

$$\mathbf{q}(\xi,\eta,\zeta,t) = \bar{\mathbf{q}}(\xi,\eta) + \epsilon\tilde{\mathbf{q}}(\xi,\eta,\zeta,t); \quad \bar{\mathbf{q}} = \mathcal{O}(1); \quad \epsilon \ll 1$$

- Harmonic Linearized Navier-Stokes Equations (HLNSE):
  - exploit basic state independence w.r.t. time and azimuthal direction
  - solution of a 2D linear system of equations

$$\tilde{\mathbf{q}}(\xi,\eta,\zeta,t) = \breve{\mathbf{q}}(\xi,\eta)\exp\left[\mathrm{i}\left(m\zeta - \omega t\right)\right]$$

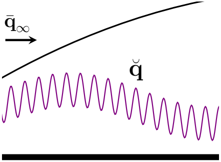

- Parabolized Stability Equations (PSE):
  - exploit slow variations in streamwise direction via separation of scales
  - parabolic integration in ξ coupled with normalization condition

$$\breve{\mathbf{q}}(\xi,\eta) = \hat{\mathbf{q}}(\xi,\eta)\theta(\xi); \; \theta(\xi) = \exp\left[\mathrm{i}\int_{\xi_0}^{\xi} \alpha(\xi')\,\mathrm{d}\xi'\right]$$

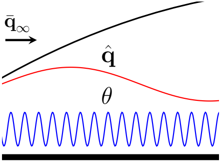

Global linear stability analysis

- Global stability analysis (GSA): HLNSE with complex $\omega \to \Omega$

$$\tilde{\mathbf{q}}(\xi, \eta, \zeta, t) = \breve{\mathbf{q}}(\xi, \eta) \exp\left[\mathrm{i}\left(m\zeta - \Omega t\right)\right]$$

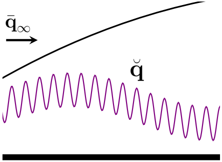

- PDE-based generalized EVP solved for each azimuthal wavenumber m:

$$\mathbf{A}\breve{\mathbf{q}} = \Omega \mathbf{B}\breve{\mathbf{q}}, \quad f = \Re(\Omega)/(2\pi)\,, \, \sigma = \Im(\Omega) \Rightarrow \begin{cases} \sigma < 0 : \text{stable} \\ \sigma > 0 : \text{unstable} \end{cases}$$